Vortex switching with discrete multivortex solitons

Daniel Leykam and Anton S. Desyatnikov
Nonlinear Physics Centre, Research School of Physics and Engineering, The Australian National University, Canberra ACT 0200, Australia
(Received 26 August 2012; published 9 October 2012)

We study the existence, stability, and dynamics of multivortex discrete solitons in a centrally coupled ring of nonlinear waveguides. A detailed analysis of possible geometrical configurations of globally linked elementary vortices within a stationary state is presented, together with the studies of their linear stability and perturbed dynamics. We identify regimes with robust switching between different vortex configurations, induced via the coordinated flipping of all vortex charges in a cluster, adiabatic spiraling of vortex lines, or spontaneous decay of unstable vortex clusters into stable solitons. These three mechanisms allow for all-optical switching between six topologically distinct vortex configurations.

DOI: 10.1103/PhysRevA.86.043812 PACS number(s): 42.65.Tg, 42.65.Pc, 42.65.Hw

I. INTRODUCTION

Topological quantities are insensitive to small perturbations such as disorder or noise, making them a promising candidate for future information storage technologies [1], data transmission [2], and quantum computation [3]. An important question is how the interaction or switching between different topological states may be controlled in these settings. The interaction between topological objects may be studied with quantized vortices [4] in optical [5,6] and matter [7] waves, which are unified by their common description with nonlinear Schrödinger-type equations [8]. The relevant topological quantity is the vortex topological charge (TC), which is the phase change in units of 2π accumulated around the vortex core.

Efficient control over TC can be achieved in periodic media, such as photonic lattices, when a vortex exchanges its orbital angular momentum with the lattice. This results in a periodic reversal of the vortex current and the switching of TC between positive and negative values, called charge flipping [9]. In general, a system possessing discrete rotational symmetry of a finite order N allows the existence and control of TC of order up to $N/2$ [10,11].

The nonlinear dynamics of vortices in periodic lattices may be studied with discrete models such as the discrete nonlinear Schrödinger equation (DNLS), which has applications in optics [12], Bose-Einstein condensates [13], protein chains [14], etc. In infinite lattices the nonlinearity supports discrete vortex solitons [15], which have been observed in optically induced lattices [16,17]. Numerous studies have explored the relationship between the stability of discrete vortex solitons and lattice geometry [18,19]. An example is the somewhat counterintuitive inverse hierarchy of stability, when the discrete vortex of higher charge is stable while its lower-order counterpart is unstable [20,21].

The simplest setting for studying the interaction between discrete vortices is a finite discrete system, such as a ring of waveguides, employed before for switching of localized optical signals [22–25]. In other fields, discrete rings have also been applied to study the coupling of nonlinear oscillations in benzene rings [26] and Bose-Einstein condensates in optical traps [13]. Recently the possibility of all-optical switching of the TC of a single vortex in a discrete ring of coupled optical waveguides was demonstrated in Ref. [27].

More generally, the states containing multiple vortices can have globally linked currents [28], so that collective effects may lead to new mechanisms for the all-optical control of TC. Multivortex solitons were introduced in hexagonal lattice systems [29] and subsequently observed in experiments in photorefractive crystals [30]. It is interesting to note recently developed analogous ideas in plasmonics [31], with multiple coupled vortices pinned to metallic nanostructures for plasmonic nanocircuit engineering with "vortex nanogear transmissions."

Motivated by recent results on multivortex solitons in a centrally coupled ring introduced in Ref. [32], we present in this paper a detailed study of the variety of multivortex states available for encoding phase information, starting with the linear limit. We show that multivortex solitons of different symmetries and TCs can be stable and discuss the relation between their stability with the discrete rotational symmetry of the structure, defined by the ring length N, the type of nonlinearity, and the coupling strength. We demonstrate three methods for achieving optically controlled switching between different vortex configurations: the spontaneous decay of unstable multivortex solitons into stable solitons or breathers, the coordinated flipping of vortex charges, and the spiraling of vortex clusters. In general, the number of different states grows rapidly with N and we identify heptamer $N = 6$ as the lowest-order structure supporting the six-state topological charge switch.

The paper is organized as follows: In Sec. II we introduce the model and discuss relevant properties such as conservation laws, definitions of discrete vortices and TC, and the classification of linear modes. Section III is devoted to a specific family of multivortex solitons constrained by the condition of uniform amplitude on the ring, which allows the solutions to be obtained analytically. The full set of asymmetric solutions can be, in principle, identified numerically; in Sec. IV we focus on multivortex solitons with definite chirality and their stability. The discussion of perturbation and instability-induced vortex switching of different states is presented in Sec. V, and Sec. VI concludes the paper.

II. DISCRETE MODEL AND LINEAR MODES

We consider a ring of N weakly coupled waveguides with Kerr nonlinearity, all coupled to a central site. We assume that the waveguides on the ring are identical, and the coupling between them can be scaled to 1 without loss of generality, while the coupling with the central site can be different, characterized by the strength C. The geometry is shown in Fig. 1(a) for the case $N = 6$. The corresponding DNLS model reads [32]

$$i\partial_z E_0 + C\sum_{n=1}^{N} E_n + \delta_0|E_0|^2 E_0 = 0, \tag{1a}$$

$$i\partial_z E_n + E_{n-1} + E_{n+1} + C E_0 + \delta_1|E_n|^2 E_n = 0, \tag{1b}$$

where the periodicity on the ring requires $E_{n+N} = E_N$ for $n = 1,2,\ldots,N$ and $\delta_{0,1} = \pm 1$ for focusing and defocusing nonlinearities in the central waveguide and on the ring.

The rate of power change at each site is given by the continuity equations

$$\frac{d|E_0|^2}{dz} = C\sum_{n=1}^{N} J_{n,0}, \tag{2a}$$

$$\frac{d|E_n|^2}{dz} = -C J_{n,0} + J_n - J_{n+1}, \tag{2b}$$

where $J_n = 2\,\mathrm{Im}(E_{n-1}^* E_n)$ is the power flow from site $n-1$ to site n, and $C J_{n,0}$ is the power flow from site n to the center, $J_{n,0} = 2\,\mathrm{Im}(E_n^* E_0)$. Equations (2) can be used to derive two integrals of motion of Eqs. (1), namely, the total power $P = \sum_{n=0}^{N}|E_n|^2$ and the Hamiltonian,

$$H = \delta_0|E_0|^4/2 + C\sum_{n=1}^{N}(E_0 E_n^* + E_0^* E_n) + \sum_{n=1}^{N}(\delta_1|E_n|^4/2 + E_n E_{n+1}^* + E_n^* E_{n+1}). \tag{3}$$

We use conservation $\partial_z P = 0$ and $\partial_z H = 0$ to monitor the accuracy of numerical simulations.

The array can be divided into N elementary triangles with vertices at sites 0, n, and $n+1$, for $n = 1,\ldots,N$. A *discrete vortex* is a circulation of power between these three sites, when three currents between sites are all nonzero and form a closed loop, e.g., for counterclockwise flow $J_n > 0$, $J_{n+1,0} > 0$, and $J_{n,0} < 0$. This condition restricts the values of phase differences between sites to the domain $(0,\pi)$, independently of (nonzero) currents amplitudes, namely, $0 < \arg(E_n^* E_{n+1}) < \pi$, $0 < \arg(E_{n+1}^* E_0) < \pi$, and $0 < \arg(E_0^* E_n) < \pi$. Therefore, the appearance of a discrete vortex can be identified using phase information only. Similar to the contour integral of phase gradient which defines the TC of a phase singularity in a continuous field [4], we introduce the TC of an elementary triangle,

$$m_n = \frac{1}{2\pi}[\arg(E_n^* E_{n+1}) + \arg(E_{n+1}^* E_0) + \arg(E_0^* E_n)]. \tag{4}$$

For nonzero amplitudes $|E_j| \neq 0$ with $j = 0,n,n+1$ the TC m_n is integer due to single valuedness of the field; otherwise the definition Eq. (4) fails due to the presence of an on-site vortex. In the example above, $0 < m_n < 3/2$ and thus $m_n = +1$ for a counterclockwise vortex. In contrast, if any two currents have opposite directions or at least one current is zero because two sites are in or out of phase, so that there is no overall circulation, then $m_n = 0$. As a three-site discrete contour, the TC of each elementary triangle may only take the values $m_n = -1,0$, or $+1$ [27]. Note also that vortices in adjacent triangles share a common segment and, therefore, cannot have the same nonzero TC, $m_n \neq m_{n+1}$ if $m_n m_{n+1} \neq 0$. We introduce the net or global TC, $M = \sum_n m_n$, which is naturally given by the topological charge of the ring, $M = \frac{1}{2\pi}\sum_{n=1}^{N}\arg(E_n^* E_{n+1})$. We note that nonzero M does not necessarily imply vortex circulation along the whole ring: The circulation is disrupted by elementary vortices of opposite charges, such as in Fig. 1(c).

In studies of the dynamics of states with multiple vortices it is useful to assign a continuous position to a phase dislocation which corresponds to each discrete vortex. Since there are many possible ways to interpolate discrete sites to form a continuous field, these positions are not unique; we use the scheme introduced in Refs. [27,32]. Using the polar coordinates (r,φ), the continuous field of a supermode $E(r,\varphi)$ is constructed as a set of linear transformations on angular sections $\varphi \in [\Theta_n,\Theta_{n+1})$ stitched together, with $\Theta_n = 2\pi n/N$ and $E_n = E(1,\Theta_n)$. The field is given by $E(r,\varphi) = E_0 + r\Psi_n(\varphi)/\sin\Theta_1$ with

$$\Psi_n(\Theta_n \leqslant \varphi < \Theta_{n+1}) = (E_{n+1} - E_0)\sin(\varphi - \Theta_n) - (E_n - E_0)\sin(\varphi - \Theta_{n+1}). \tag{5}$$

An example of continuous phase of the supermode is shown in Fig. 1(b); we use this continuous field to calculate the positions of phase singularities, shown in Fig. 1(c) and below as red (gray) and blue (dark gray) circles for TC equal $+1$ and -1, respectively.

We look for stationary solutions with propagation constant k, $E_0 = Ae^{ikz}$ and $E_n = B_n e^{ikz}$. The global phase invariance can be used to reduce the number of variables, and we set $A \geqslant 0$ without loss of generality. Substitution into Eq. (1) gives the stationary equations

$$(k - \delta_0 A^2)A = C\sum_{n=1}^{N} B_n, \tag{6a}$$

$$(k - \delta_1|B_n|^2)B_n = CA + B_{n-1} + B_{n+1}. \tag{6b}$$

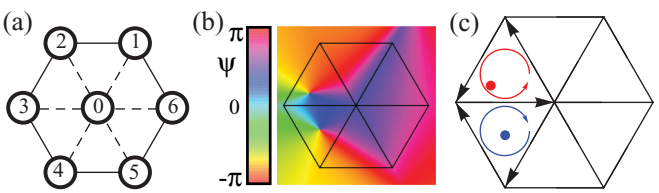

FIG. 1. (Color online) (a) Sketch of $N = 6$ ring coupled to a central waveguide. (b) An example of the phase profile $\arg(E)$ interpolated with Eq. (5) for a particular set of amplitudes $\{E_n\}$; corresponding vortex currents are shown with black arrows in (c) with phase dislocations of topological charge $+1$ (-1) indicated with red/gray (blue/dark gray) dots and counterclockwise (clockwise) arrows, respectively.

As $C \to \infty$, the coupling between the ring sites becomes negligible. Coupling only occurs from the ring to the center, so balanced current loops cannot form and vortex solitons do not exist. Therefore vortex solitons will only exist in this system with the coupling below a critical value of C. On the other hand, as $C \to 0$, the model reduces to the simple ring system studied in Ref. [27]. In this case, each site on the ring is coupled only to its two neighbors, and for any stationary state the continuity requires $J_n = J_{n+1}$, thus near the limit $C \to 0$ any multivortex solitons must have nonzero global charge M.

The linear modes of the system are obtained by setting $\delta_{0,1} = 0$ in Eqs. (6) and using the discrete Fourier transform pair

$$B_n = \sum_{s=-N/2}^{N/2} F_s e^{i\Theta_s n}, \quad F_s = \frac{1}{N}\sum_{n=1}^{N} B_n e^{-i\Theta_s n},$$

where F_s are the Fourier amplitudes and s takes integer values. Transforming Eq. (6) gives a system of equations for the Fourier amplitudes

$$F_s(k - 2\cos\Theta_s) = 0, \quad s \neq 0, \tag{7a}$$
$$F_0(k-2) = CA, \tag{7b}$$
$$F_0 NC = kA. \tag{7c}$$

There are two distinct classes of solutions.

(i) *Vortex-free* modes have $F_s = 0$ for all $s \neq 0$, while A and F_0 are nonzero and satisfy

$$k_\pm = 1 \pm \sqrt{1 + NC^2} = NCF_0/A. \tag{8}$$

All amplitudes are real and hence there is no power flow between sites. The k_+ mode has all sites oscillating in phase, while the k_- mode has the central site π out of phase with the ring. For both modes the central coupling C controls both the propagation constant k and the amplitude of the ring sites F_0 relative to the center A.

(ii) *On-site vortex* modes have $k = k_m = 2\cos\Theta_m$, with $|m| < N/2$, $F_s = 0$ for $s \neq m$, $A = 0$, and arbitrary F_m. The central site hosts a vortex with TC $M = m$ and there is no power flow between the ring and the center, so the modes are independent of C.

We consider in Fig. 2 the case $N = 5$ and plot the linear mode eigenvalues in Fig. 2(a) versus coupling C. Note the crossing of k_- and k_2 modes at $C \approx 1.1$, similar to the crossings observed for $N = 6$ in Ref. [32]. At such points, we can construct stationary *multivortex modes* as superpositions of the form

$$E_n = [F_0 + r_1 \exp(i\Theta_m n + i\phi_1) + r_2 \exp(-i\Theta_m n + i\phi_2)]e^{ikz}, \tag{9}$$

taking into account the degeneracy $k = k_- = k_{\pm m}$. The arbitrary relative amplitudes $r_{1,2}$ and phases $\phi_{1,2}$ control the global TC, as we show in Fig. 2(b). A superposition of $m = \pm 2$ vortices and the out-of-phase mode can even result in modes with global TC $|M| = 1$. Hence the global TC is no longer tied to the discrete rotational symmetry of the mode. Examples of vortex configurations with net charges $M = 0$, 1, and 2 are shown in Fig. 2(c). They are obtained by varying only the phase ϕ_1 with all other parameters fixed. Note that no intersections occur with the k_1 mode in Fig. 2(a), thus this mode cannot form multivortex states. In general, no crossings occur when $0 < k_{|m|} < 2$, so multivortex modes are restricted to $N/4 \leqslant |m| \leqslant N/2$.

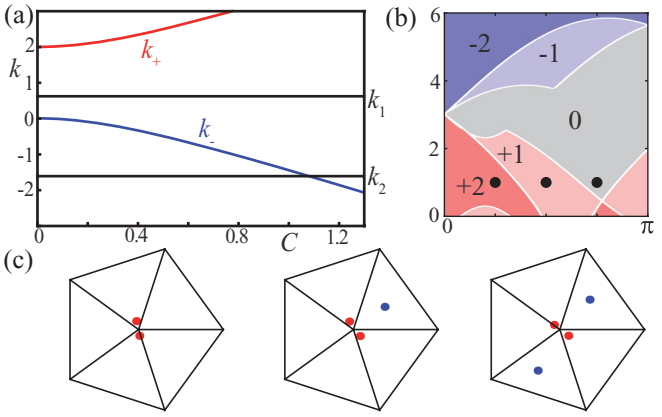

FIG. 2. (Color online) (a) Wave numbers k of linear modes as a function of the central coupling C for an $N = 5$ array. The in- and out-of-phase modes $k_\pm$ are shown with red (gray) and blue (dark gray) lines, while the vortex modes are in black. (b) Global TC M of the stationary multivortex modes Eq. (9) shown as signed integers in shaded domains of the plane (r_2, ϕ_1) for fixed parameters $C \approx 1.1$, $r_1 = 3$, and $\phi_2 = 0$. (c) Vortex configurations of the modes indicated by black circles with $r_2 = 1$ in (b).

The on-site vortex modes are effectively invariant under discrete rotations, which merely result in a shift in their global phase. In contrast, the multivortex modes have an *asymmetric* phase profile on the ring, and discrete rotations can result in a distinct state, with the individual vortices occupying different elementary triangles. Of course, such solutions are trivially degenerate, and in the following we do not distinguish between them as separate solutions. However, this distinction will become important when we discuss vortex switching in Sec. V.

III. CONSTANT AMPLITUDE SOLITONS

The linear modes serve as a starting point for the study of nonlinear solutions to Eq. (6). Here we consider in detail the particular class of solutions introduced in Ref. [32] under the simplifying assumption of constant amplitude on the ring, $B_n = Be^{i\psi_n}$. This assumption is similar to the separation of radial and azimuthal variables in a continuous system [33,34] as it allows the separation of the nonlinear part $\sim B^2$ in Eq. (6). The unknown phase factors $e^{i\psi_n}$ satisfy effectively linear equations which can be solved by applying the discrete Fourier transform, $e^{i\psi_n} = \sum_{s=-N/2}^{N/2} p_s e^{i\Theta_s n}$, where p_s are Fourier amplitudes. The transformed equations are

$$Bp_s(k - \delta_1 B^2 - 2\cos\Theta_s) = 0, \quad s \neq 0, \tag{10a}$$
$$Bp_0(k - \delta_1 B^2 - 2) = CA, \tag{10b}$$
$$Bp_0 NC = (k - \delta_0 A^2)A. \tag{10c}$$

The *vortex-free solitons* bifurcate from the in- and out-of-phase modes in the linear limit above, with $p_s = 0$ for $s \neq 0$

and the two roots $k_\pm$ satisfying

$$(k-\delta_0 A^2)(k-\delta_1 B^2-2)=C^2 N. \tag{11}$$

The *on-site vortex solitons* are the roots of Eqs. (10) with $A=0, k=k_m=\delta_1 B^2+2\cos\Theta_m$, similar to the ring solitons studied in Ref. [27]. Their stability is affected by the coupling strength C.

The third class of solutions are *multivortex solitons* [32], the roots of Eq. (10) with $k=k_m$ and nonzero p_0, A satisfying

$$Bp_0(\cos\Theta_m-1)=CA/2, \tag{12a}$$

$$Bp_0NC=(2\cos\Theta_m+\delta_1 B^2-\delta_0 A^2)A. \tag{12b}$$

When $k=k_m$ the left-hand side of Eq. (10a) vanishes for $|s|=m$, leaving p_m and p_{-m} as free variables. The general form of the phase term $\exp(i\psi_n)$ is hence

$$e^{i\psi_n}=p_0+p_+e^{i\Theta_m n}+p_-e^{-i\Theta_m n}, \tag{13}$$

where $p_\pm$ are complex constants. As in the linear case, the multivortex solutions appear as a superposition of ordinary vortices and a vortex-free state. However, there is an additional constraint that $|e^{i\psi_n}|=1$ for all n, which restricts the values of $p_\pm$.

The question of when this constraint can be satisfied may be answered with the help of a change of variables. Writing the complex parameters $p_\pm$ in terms of four real parameters, $p_\pm=\beta_\pm e^{i\chi_\pm}$, and introducing the variables $t=\Theta_m n-t_0$ and $t_0=(\chi_--\chi_+)/2$, the constraint equation takes the form

$$|e^{i\psi_n}|^2=1=\frac{(x-x_0)^2}{w_x^2}+\frac{(y-y_0)^2}{w_y^2}, \tag{14}$$

with $x=\cos t$ and $y=\sin t$ on the unit circle and $x_0=-w_x p_0\cos\chi$, $y_0=-w_y p_0\sin\chi$, $w_{x,y}=1/(\beta_-\pm\beta_+)$, and $\chi=-(\chi_++\chi_-)/2$. We see now that the constraint has a simple geometrical interpretation—it is the equation for an ellipse in the variables x and y. However, x and y are constrained to lie on a unit circle, so the constraint is only satisfied at points where the ellipse intersects the unit circle. We see from the definitions of x, y, and t that, as n ranges from 1 to N, the pair (x,y) generates $N/|m|$ distinct points. Ignoring the degenerate case $A=0$ (when the ellipse is precisely the unit circle, corresponding to the on-site vortex solitons), an ellipse can have at most four intersections with a circle. Hence the constant amplitude multivortex solitons are limited to $N/|m|=2,3$, or 4. The distinct vortex configurations allowed are presented in Fig. 3.

Particularly interesting is the $N/|m|=3$ soliton, which must satisfy the constraint equations

$$e^{i\psi_1}+e^{i\psi_2}+e^{i\psi_3}=-CA/B, \tag{15a}$$

$$k=\delta_1 B^2-1=\delta_0 A^2-NC^2/3. \tag{15b}$$

The complex Eq. (15a) is equivalent to two real constraints to the phases $\psi_{1,2,3}$, leaving one of the phases as a *free parameter*, independent of nonlinearity. Instead of a single soliton, there is a one-parameter family of solitons with the free phase ψ_1; the corresponding Hamiltonian is

$$H=\delta_0 A^4/2+N(\delta_1 B^4/2-B^2-C^2A^2/3), \tag{16}$$

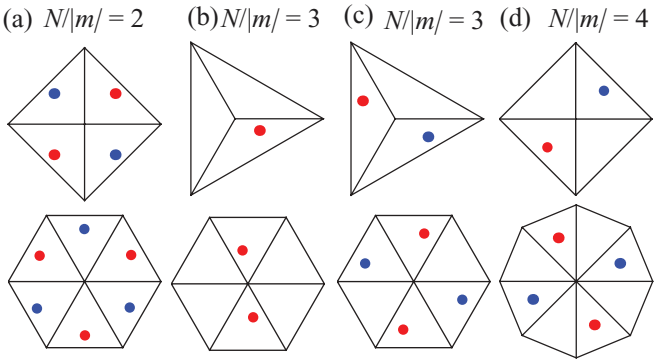

FIG. 3. (Color online) Topology of different solitons with constant amplitude on the ring, the ratio $N/|m|=2$ in column (a), $N/|m|=3$ in (b) (small C) and (c) (large C), and $N/|m|=4$ in column (d).

and it is independent of the choice of free phase. Therefore the family is degenerate, as all members share the same power and Hamiltonian.

The degeneracy of solutions above has interesting consequences on the structure of soliton family, determined by the source term CA/B in Eq. (15a). When $CA/B<1$ (weak central coupling), all elementary vortices have the same charge, giving a global charge of $|M|=N/3$ [see Fig. 3(b)]. In contrast, for strong central coupling $CA/B>1$, the oppositely charged vortices appear, giving the whole cluster a net charge of 0, i.e., no overall circulation of energy along the ring. Despite the fact that there is no current loop on the ring, the arrangement of elementary vortices can produce a chiral structure [see the top of Fig. 3(c)]. Furthermore, the value of CA/B determines the shape of lines traced by vortex positions as parameters change; examples are shown in Fig. 4.

Another consequence of the degeneracy of solutions is that, when such a soliton is stable, in addition to high-frequency oscillations in the vortex positions, perturbations and noise can produce an adiabatic drift of vortices through all members of the family along the transverse trajectories in Fig. 4. This effect was described in Ref. [32] as *cyclic charge flipping*.

The linear stability of solitons with the uniform amplitude on the ring can be considered analytically, similar to the stability of the discrete vortices without central coupling [27]. However, the resulting eigenvalue problems, while analytically tractable, do not take a particularly simple or enlightening form. Therefore, we employ numerical eigensolvers to determine linear stability of particular solitons. As a particular example, we contrast the existence, stability, and bifurcations of multivortex solitons with self-focusing nonlinearity $\delta_{0,1}=1$

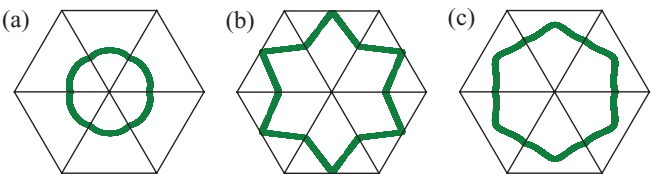

FIG. 4. (Color online) Vortex positions traced by members of the soliton family with $N=6$ and $|m|=2$ when the free parameter ψ_1 changes. The ratio $CA/B=0.35$ in (a), 1.04 in (b), and 1.73 in (c).

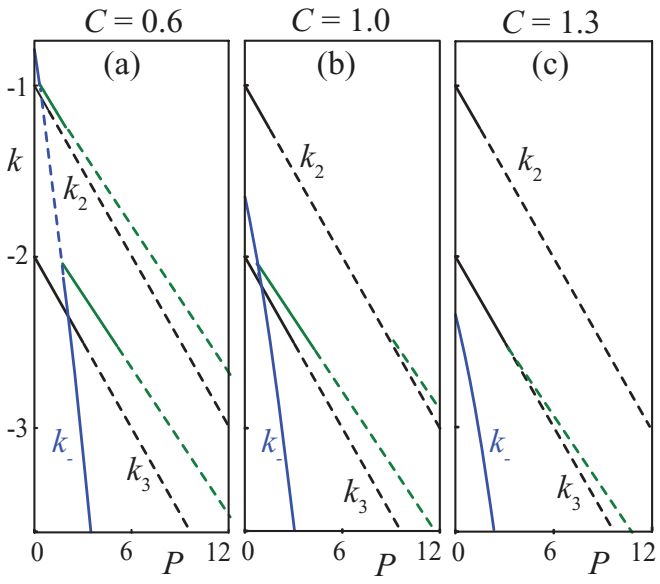

FIG. 5. (Color online) Existence and stability diagrams for constant amplitude solitons with defocusing nonlinearities $\delta_{0,1} = -1$ and different values of coupling C, cf. self-focusing case in Fig. 2 of Ref. [32]. Solid and dashed lines indicate linearly stable and unstable solitons, respectively. Blue, black, and green curves correspond to the out-of-phase, vortex, and multivortex solitons respectively. Note in (b) an instability region in the k_- branch at the first bifurcation point is not visible at this scale, and in (c) the bifurcation of the $m = 2$ multivortex soliton from the k_2 branch does not occur within the range of the plot.

in Ref. [32] and multivortex solitons in a heptamer $N = 6$ with defocusing nonlinearities $\delta_{0,1} = -1$ in Fig. 5.

In contrast to the linear multivortex modes at specific values of C, the multivortex solitons exist over a continuous range of C. For focusing nonlinearities $\delta_{0,1} = 1$ they bifurcate from their parent single-vortex soliton for $C < C_{\rm crit} = 2|\sin(\Theta_m/2)|\sqrt{-2\cos\Theta_m/N}$. At $C_{\rm crit}$ the corresponding linear multivortex mode appears, the bifurcation occurs from the linear limit, and the soliton phase profile becomes independent of its total power. For $C > C_{\rm crit}$ the bifurcation occurs from the out-of-phase soliton. In contrast, in the case $\delta_{0,1} = -1$, illustrated in Fig. 5, the bifurcation structure is reversed and instabilities occur at lower power.

For both types of nonlinearity, the multivortex solitons steal stability from their parent soliton at the point of bifurcation, characteristic of a transcritical bifurcation. The other halves of the multivortex branches exist in the mixed nonlinearity cases where δ_0 and δ_1 take different signs, and they can be stable (not shown). At high power, for all values of C, the constant amplitude multivortex solitons are linearly unstable, except for the $N/|m| = 2$ soliton when $\delta_{0,1} = 1$. We attribute its stability to the fact that all elementary triangles are occupied by vortices. As vortices are removed, resulting in the $N/|m| = 3$ and $N/|m| = 4$ solitons, instability appears at lower power.

Finally, while the highly symmetric nature of Eq. (1) allowed us to obtain these solitons analytically, we observe that they can also persist as stable solitons in the presence of significant anisotropy (up to 20%). We considered anisotropic central coupling $C \to C_n$ and also anisotropy in the coupling on the ring. Anisotropy breaks the degeneracy of the family defined by Eq. (15a), so adiabatic rotation of the vortices is suppressed. However, rotation may still be observed if a sufficiently large perturbation is applied to the soliton.

IV. CHIRAL SOLITONS

The constant amplitude solitons form only a very small subset of the multivortex solitons supported by this system, as they are limited to ring sizes N a multiple of 2 or 3 and global TC of 0 or $|N/3|$. To obtain the other stationary solutions, Eq. (6) must be solved numerically. We find solutions using the Newton-Raphson method and present examples of some stable solitons in Fig. 6.

A common feature of these solitons is the presence of an axis of symmetry and no discrete rotational symmetry. The lack of discrete rotational symmetry means that solitons with zero global TC can still be chiral states. Symmetric solitons have identical site amplitudes about the symmetry axis, which results in inverted vortex charges about the axis. Unless a vortex lies on the symmetry axis, then for every charge 1 vortex, there is a charge -1 vortex, so symmetric solitons have low global TC.

Antisymmetric solitons have identical site amplitudes about the symmetry axis after complex conjugation, so vortex charges are identical on either side of the symmetry axis. At low C, their ring phase profile resembles that of a simple ring vortex of charge m. The phases and amplitudes are slightly perturbed due to the central coupling, which splits the charge m on-site vortex into m charge 1 vortices. Similar to the $N/|m| = 3$ constant amplitude soliton, there is a free parameter which allows spiraling of vortices during propagation. Above a critical value of C, vortices of opposite charge appear, giving

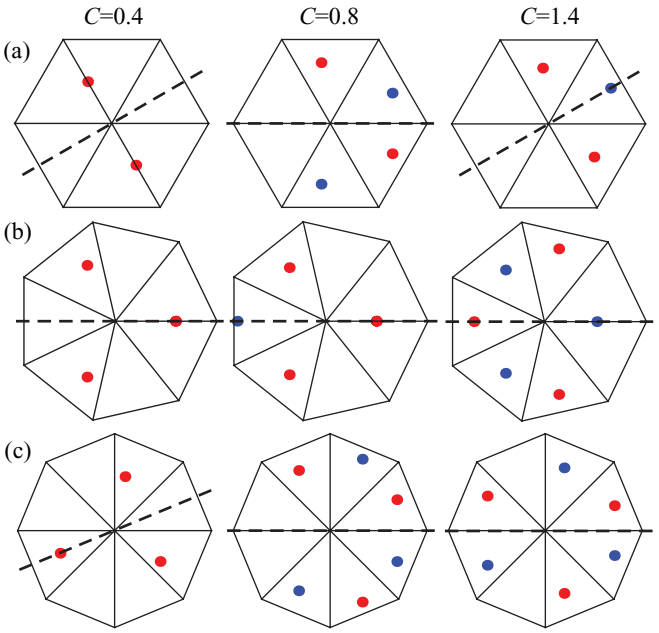

FIG. 6. (Color online) Examples of multivortex solitons with an axis of symmetry (dashed line) stable at high power, $\delta_{0,1} = 1$. (a) $N = 6$. (b) $N = 7$. (c) $N = 8$.

the asymmetric solitons lower net charge, but vortex spiralling can still occur. At sufficiently high C spiralling is suppressed.

An important difference between rings with odd and even N is the location of the symmetry axis. When N is odd, the symmetry axis must pass through one of the ring sites, while for even N the axis can pass either between two pairs of ring sites, or through a single pair, which permits additional vortex configurations.

While we have also found examples of solitons with fewer vortices (and more spread out) than those in Fig. 6, they tend to be unstable. The $C = 1.4$ soliton in Fig. 6(c) is protected from decay, because placing a vortex in an unoccupied triangle would result in two adjacent vortices of the same charge, which is forbidden. In contrast, solitons such as those in Fig. 6(a), $C = 0.8, 1.4$, are only stable when corners not adjacent to any vortices have a small amplitude compared to the rest of the ring. The equivalent high-amplitude configurations are unstable. High- and low-amplitude configurations appear together at a saddle-node bifurcation.

The solutions found using the Newton-Raphson method are sensitive to the initial conditions used in the procedure. Therefore, we also look for solitons using a more systematic approach, by solving the current balance equations, such as what was used in Ref. [9]. We searched for other solutions in an $N = 6$ ring.

Surprisingly, we find an example of a stable, *completely asymmetric* soliton. Its phase profile is shown in Fig. 7(a). Inside the ring there are two charge 1 vortices, giving the soliton a net charge of 2. A third, oppositely charged vortex is located in the supermode just outside the ring. This soliton appears at a saddle-node bifurcation. The two branches have very similar phase profiles—the unstable branch has a vortex located at the boundary between two elementary triangles, while this vortex is slightly displaced in the stable branch. Instability occurs when the exterior vortex enters the ring, setting up a new circulation of energy.

We do not find any stable solutions at high power for defocusing nonlinearity $\delta_{0,1} = -1$. The reason for this is that in a simple ring decoupled from the central site, such as that studied in Ref. [27], at high power all eigenvalues for vortex solitons are either stable or unstable. Therefore solitons unstable for focusing nonlinearity become stable when the nonlinearity sign is reversed. For the centrally coupled ring, reversing the nonlinearity still swaps the stability of all the eigenvalues. But instabilities in this case only appear in some of the eigenvalues. Hence swapping all signs does not change overall stability.

We observe qualitatively similar existence and stability properties for other values of N and C. We have searched up to $N = 15$. Below a critical value of C, multivortex solitons with high TC are stable, in agreement with the limit $C \to 0$ studied in Ref. [27].

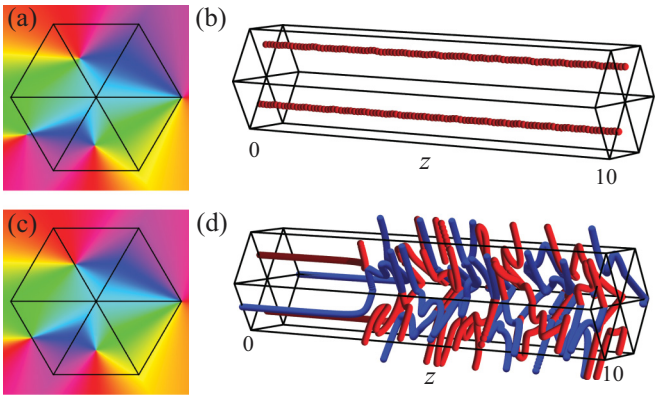

FIG. 7. (Color online) (a) Interpolated phase profile of the stable asymmetric multivortex soliton at $k = 30$. (b) Stable vortex lines under a 1% perturbation. (c) Phase profile of the unstable branch at $k = 30$. (d) Unstable vortex lines under a 0.01% perturbation.

V. SOLITON DYNAMICS AND VORTEX SWITCHING

In this section we explore ways in which the system under consideration can be used to achieve controlled transitions between different vortex configurations, starting with the dynamics of unstable solitons.

The dynamics of an unstable $N = 7$, $C = 1.4$ symmetric soliton are shown in Fig. 8. While there is one triangle without a vortex, filling the empty triangle is forbidden because it would result in adjacent vortices of like charge. The plot of the power in Fig. 8(b) demonstrates that the soliton is unstable. A perturbation induced by small numerical errors accumulated while solving the propagation equation grows exponentially to large oscillations within a distance of $\Delta z = 10$. However, on average the power at each site remains unchanged. The reconstructed vortex lines in Fig. 8(c) show relatively weaker oscillations. At the onset on instability at $z \approx 10$, the vortex positions shift, then they oscillate about new equilibrium positions, shown in Fig. 8(d). Comparing the initial and final states, we see that the positive vortex next to the empty triangle moves to the boundary, resulting in two "half occupied" triangles. This is accompanied by a rotation of the symmetry axis by $\pi/7$, and the configuration becomes antisymmetric.

Decay can also occur via a negative vortex moving to a triangle boundary, which rotates the symmetry axis in the opposite direction. The final state then has opposite chirality. If we start with the exact symmetric soliton solution, then which

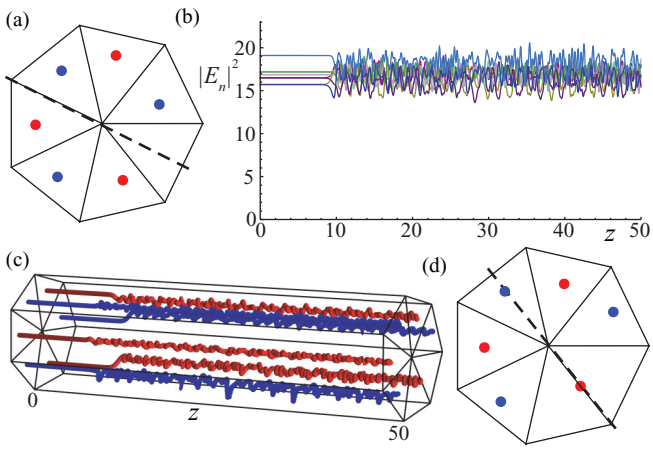

FIG. 8. (Color online) Spontaneous decay of an $N = 7$ symmetric soliton at $C = 1.4$ to an antisymmetric soliton. (a) Initial vortex configuration. (b) Power at each site during propagation (different sites are different colours) over a distance $L = 50$. (c) Vortex lines during propagation. (d) Final vortex configuration.

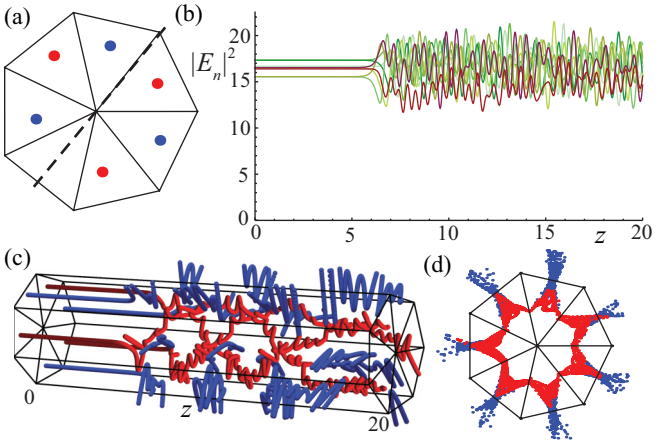

FIG. 9. (Color online) Spontaneous decay of an uncharged $N = 7$ symmetric soliton ($C = 0.8$) to a charged breather. (a) Initial vortex configuration. (b) Power at each site during propagation (different sites are different colours) over a distance $L = 50$. (c) Vortex lines during propagation. (d) Vortex positions during propagation projected onto a plane.

decay occurs is unpredictable and sensitive to noise. However, an appropriate perturbation to the soliton may be used to push the soliton to the desired output configuration, even in the presence of noise.

If coupling is reduced to $C = 0.8$, the instability dynamics of the symmetric soliton is quite different; it is illustrated in Fig. 9. Following the decay, the site powers still oscillate about constant average values, however, the vortex behavior is more complex. Vortices of charge -1 repeatedly leave and enter the ring, while charge $+1$ vortices move at irregular intervals. The vortex lines in Fig. 9(c) do not show an obvious final, equilibrium state. However, projecting the vortex positions at different z values onto a plane in Fig. 9(d), we see surprising order in the dynamics. The charge 1 vortices rotate about the central site, while the -1 vortices appear only briefly at the edge of the ring. The soliton has hence collapsed to a stable charge (2 or 3) breather. The chirality of initial state with global charge 0 is proven, as reversing its chirality results in a negative charge breather.

We stress that the transition of multivortex solitons to other regular states does not occur for all unstable configurations, and only occurs at sufficiently high power, while at lower powers we still observe irregular dynamics.

Switching between different vortex configurations may also be achieved by applying large perturbations to stable solitons. As an example, we consider encoding a signal modulated in the power of a laser beam into multivortex states. This may be achieved by passing an input beam of total power P through a phase mask to create the appropriate phase profile, and then propagating it through a waveguide coupler of fixed length. The input phases are chosen to correspond to a stable constant amplitude multivortex soliton with power $P_0 = |A|^2 + N|B|^2$. Changing the input power $P = \alpha^2 P_0$ scales the site amplitudes to αA and αB, resulting in a nonstationary state with vortex dynamics. We focus on switching in an $N = 6$ ring.

There are two mechanisms which may be used to control the TC of stable multivortex solitons: *coordinated charge flipping*, in which all discrete vortices reverse their charges simultaneously via hyperbolic avoided crossings, and *cyclic charge flipping*, in which vortex lines spiral around the central site during propagation [32].

Coordinated charge flipping can occur both in the constant amplitude and chiral solitons. The total power controls the charge flipping frequency, and hence the output state after propagation through a coupler of fixed length. The oscillations are periodic, thus by choosing the right input powers it is possible to switch vortex charges while leaving the power in the individual waveguides unchanged. As an example we show coordinated charge flipping of the $N = 6, m = 2$ soliton in Figs. 10(a) and 10(b). The adiabatic spiraling of vortices is suppressed by perturbing the input phase profile such that $\psi_2 = \psi_3$, with ψ_1 chosen such that the power flows are almost balanced. This results in small-amplitude oscillations at full input power, with the symmetry of the phases $\psi_2 = \psi_3$ preventing any rotation.

When the input power is strongly detuned from its stationary state, large oscillations occur and a coordinated reversal of the vortex currents is achieved. The symmetry on the ring is preserved during the oscillations—sites 2, 3, 5, and 6 all oscillate together in Fig. 10(b) (the purple/dark gray curve). A consequence of this symmetry is that the amplitudes do not return to their original levels at equally spaced intervals. The constant amplitude is restored at $z \approx 14, 24, 38, \ldots$, so there are two alternating periods: $\Delta z = 14$ and $\Delta z = 10$. The output

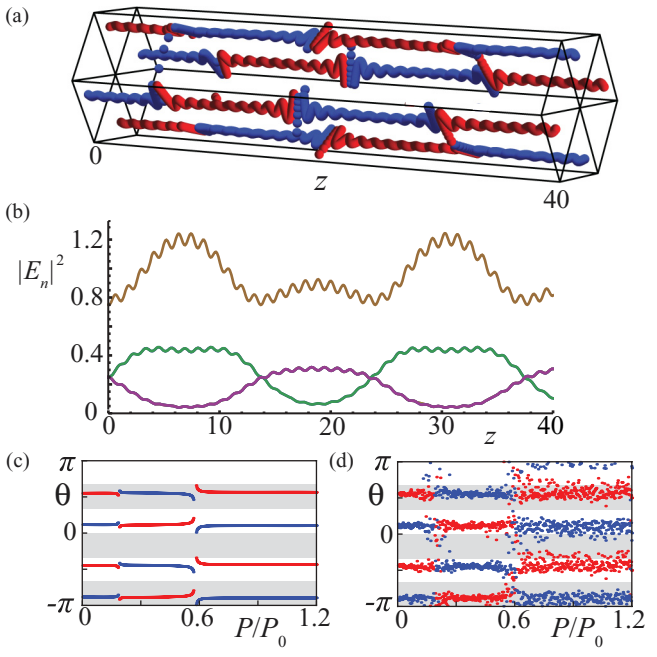

FIG. 10. (Color online) Vortex lines (a) and site powers $|E_n|^2$ (b) during coordinated charge flipping in a seven waveguide coupler, $C = 1$, $L = 40$, $P/P_0 = 0.5$ and the input phases defined by $\psi_1 = 1.5$ and $\psi_2 = \psi_3 = 3.65$. (c,d) Output vortex angles from an $L = 10$ coupler as a function of the input power. Different elementary triangles are shown as alternating white and grey backgrounds. (c) No noise and (d) 20% noise applied to input amplitudes and phases with total power conserved.

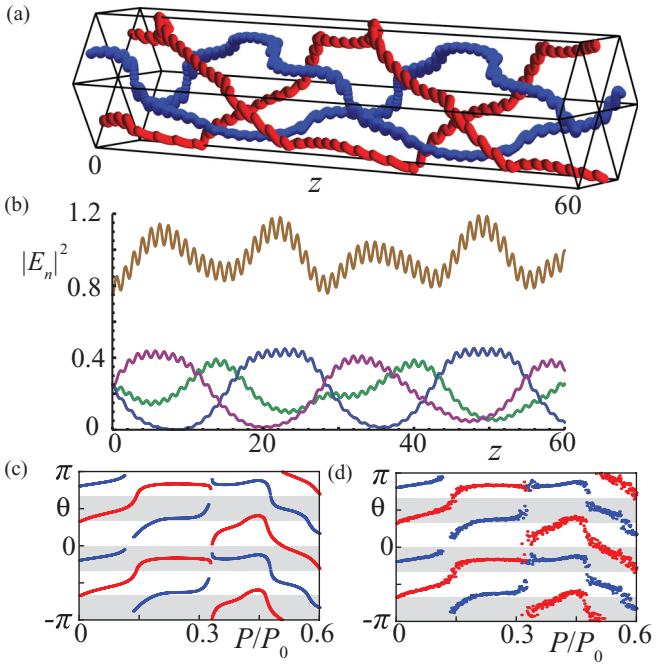

FIG. 11. (Color online) Vortex lines (a) and site powers (b) during cyclic charge flipping. $C = 1, L = 60, \psi_1 = \pi, \psi_2 = 4.33, \psi_3 = 1.95, k = -0.5, P/P_0 = 0.5$. (c,d) Output vortex angles from an $L = 20$ coupler as a function of input power. Different elementary triangles are shown as alternating white and grey backgrounds. (c) No noise and (d) 5% noise applied to input amplitudes and phases with total power conserved.

vortex configuration from a device of fixed length $L = 10$ is shown in Fig. 10(c). The vortex charges flip back and forth as the power is increased, realizing a two-state multivortex switch. Figure 10(d) shows how this switching is robust to noise.

If the symmetry $\psi_2 = \psi_3$ is then broken, it is possible to achieve further control of the output multivortex state through cyclic charge flipping. We show the dynamics of the $N = 6$, $m = 2$ soliton under a strong perturbation to the input power in Figs. 11(a) and 11(b). The vortex dynamics are qualitatively different from the smooth adiabatic spiraling demonstrated in Ref. [32]. A "discrete rotation" of the vortices is observed, in which the vortices spend most of the time at fixed angular positions, with short periods of rapid rotation. This behavior is also visible in the switching characteristics of the device in Fig. 11(c), with the output angles remaining almost constant as P is increased, until sudden switching occurs. This discrete rotation results in good performance of the switch under noise, as we show in Fig. 11(d).

With these two mechanisms, the all-optical switching between the six distinct TC configurations of the $N = 6$, $m = 2$ soliton is supported. This may be used to design a six-state multivortex switch. We stress that this is just one example of switching supported by perturbed multivortex solitons. Switching properties may be more finely tuned through the choice of input phases, k, C, the device length L, and the method of perturbation. Switching based on vortex spiraling may also be achieved for other values of N using the charged chiral solitons presented in Figs. 6(b) and 6(c).

VI. CONCLUSION

We have studied the existence and stability of multivortex solitons in a centrally coupled discrete ring and found that a rich variety of stable solitons possessing different symmetries exist for focusing nonlinearity. Stable solitons possessing the full range of topological charges permitted by the discrete symmetries of the system are supported. In contrast, for defocusing nonlinearity all multivortex solitons were unstable above a critical power.

We showed that the combination of nonlinearity and the interaction between vortices provides three mechanisms for the all-optical control of TC: spontaneous decay of solitons, coordinated charge flipping, and cyclic charge flipping. As an example we showed that the latter two mechanisms could be used for all-optical switching between six topologically distinct vortex configurations. This offers a significant improvement over previous switching mechanisms based on single-vortex states and allows multichannel information processing.

Since the multivortex solitons occur as a nonlinear superposition of ordinary vortex solitons with different chiralities, an interesting question is how the chiral solitons we have described here would behave in a chiral system, e.g., if the waveguides are twisted [35,36].

ACKNOWLEDGMENT

This work is supported by the Australian Research Council.

[1] Z. Dutton and J. Ruostekoski, Phys. Rev. Lett. **93**, 193602 (2004).
[2] G. Gibson, J. Courtial, M. Padgett, M. Vasnetsov, V. Pasko, S. Barnett, and S. Franke-Arnold, Opt. Express **12**, 5448 (2004).
[3] C. Nayak, S. H. Simon, A. Stern, M. Freedman, and S. Das Sarma, Rev. Mod. Phys. **80**, 1083 (2008).
[4] J. F. Nye and M. V. Berry, Proc. R. Soc. London, Ser. A **336**, 165 (1974).
[5] M. S. Soskin and M. V. Vasnetsov, Prog. Opt. **42**, 219 (2001).
[6] M. R. Dennis, K. O'Holleran, and M. J. Padgett, Prog. Opt. **52**, 293 (2009).
[7] J. E. Williams and M. J. Holland, Nature (London) **401**, 568 (1999).
[8] A. S. Desyatnikov, Yu. S. Kivshar, and L. Torner, Prog. Opt. **47**, 291 (2005).
[9] T. J. Alexander, A. A. Sukhorukov, and Yu. S. Kivshar, Phys. Rev. Lett. **93**, 063901 (2004).
[10] A. Ferrando, M. Zacarés, M.-A. García-March, J. A. Monsoriu, and P. F. de Córdoba, Phys. Rev. Lett. **95**, 123901 (2005).

[11] M.-A. García-March, A. Ferrando, M. Zacarés, S. Sahu, and D. E. Ceballos-Herrera, Phys. Rev. A **79**, 053820 (2009).
[12] D. N. Christodoulides and R. I. Joseph, Opt. Lett. **13**, 794 (1988).
[13] A. Trombettoni and A. Smerzi, Phys. Rev. Lett. **86**, 2353 (2001).
[14] N. Molkenthin, S. Hu, and A. J. Niemi, Phys. Rev. Lett. **106**, 078102 (2011).
[15] B. A. Malomed and P. G. Kevrekidis, Phys. Rev. E **64**, 026601 (2001).
[16] D. N. Neshev, T. J. Alexander, E. A. Ostrovskaya, Y. S. Kivshar, H. Martin, I. Makasyuk, and Z. Chen, Phys. Rev. Lett. **92**, 123903 (2004).
[17] J. W. Fleischer, G. Bartal, O. Cohen, O. Manela, M. Segev, J. Hudock, and D. N. Christodoulides, Phys. Rev. Lett. **92**, 123904 (2004).
[18] D. Pelinovsky, P. Kevrekidis, and D. Frantzeskakis, Physica D **212**, 20 (2005).
[19] F. Lederer, G. I. Stegeman, D. N. Christodoulides, G. Assanto, M. Segev, and Y. Silberberg, Phys. Rep. **463**, 1 (2008).
[20] B. Terhalle, T. Richter, K. J. H. Law, D. Göries, P. Rose, T. J. Alexander, P. G. Kevrekidis, A. S. Desyatnikov, W. Krolikowski, F. Kaiser, C. Denz, and Yu. S. Kivshar, Phys. Rev. A **79**, 043821 (2009).
[21] K. J. H. Law, D. Song, P. G. Kevrekidis, J. Xu, and Z. Chen, Phys. Rev. A **80**, 063817 (2009).
[22] J. Hudgings, L. Molter, and M. Dutta, IEEE J. Quantum Electron. **36**, 1438 (2000).
[23] C. N. Alexeyev, A. V. Volyar, and M. A. Yavorsky, Phys. Rev. A **80**, 063821 (2009); **84**, 063845 (2011).
[24] W. Królikowski and Yu. S. Kivshar, J. Opt. Soc. Am. B **13**, 876 (1996).
[25] K. Hizanidis, S. Droulias, I. Tsopelas, N. K. Efremidis, and D. N. Christodoulides, Int. J. Bifurcation Chaos **16**, 1739 (2006).
[26] J. Eilbeck, P. Lomdahl, and A. Scott, Physica D **16**, 318 (1985).
[27] A. S. Desyatnikov, M. R. Dennis, and A. Ferrando, Phys. Rev. A **83**, 063822 (2011).
[28] L.-C. Crasovan, G. Molina-Terriza, J. P. Torres, L. Torner, V. M. Pérez-García, and D. Mihalache, Phys. Rev. E **66**, 036612 (2002).
[29] T. J. Alexander, A. S. Desyatnikov, and Yu. S. Kivshar, Opt. Lett. **32**, 1293 (2007).
[30] B. Terhalle, T. Richter, A. S. Desyatnikov, D. N. Neshev, W. Krolikowski, F. Kaiser, C. Denz, and Yu. S. Kivshar, Phys. Rev. Lett. **101**, 013903 (2008).
[31] S. V. Boriskina and B. M. Reinhard, Nanoscale **4**, 76 (2012).
[32] D. Leykam and A. S. Desyatnikov, Opt. Lett. **36**, 4806 (2011).
[33] A. S. Desyatnikov and Yu. S. Kivshar, Phys. Rev. Lett. **88**, 053901 (2002).
[34] A. S. Desyatnikov, A. A. Sukhorukov, and Yu. S. Kivshar, Phys. Rev. Lett. **95**, 203904 (2005).
[35] S. Longhi, J. Phys. B **40**, 4477 (2007).
[36] J. Becker, P. Rose, M. Boguslawksi, and C. Denz, Opt. Express **19**, 9848 (2011).